Experimental Optical Simulator of Reconfigurable and Complex Quantum Environment

P. Renault,[1,*,†] J. Nokkala,[2] G. Roeland,[1] N.Y. Joly,[5,6,7] R. Zambrini,[3] S. Maniscalco,[4] J. Piilo,[2] N. Treps,[1] and V. Parigi[1]

[1] *Laboratoire Kastler Brossel, Sorbonne Université, CNRS, ENS-Université PSL, Collège de France, Paris 75005, France*

[2] *Department of Physics and Astronomy, University of Turku, Turun yliopisto FI-20014, Finland*

[3] *Instituto de Física Interdisciplinar y Sistemas Complejos IFISC (CSIC-UIB), Campus Universitat Illes Balears, Palma de Mallorca E-07122, Spain*

[4] *QTF Centre of Excellence, Department of Physics, University of Helsinki, P.O. Box 43, Helsinki FI-00014, Finland*

[5] *Department of Physics, Friedrich-Alexander-Universität, Staudtstraße 2, Erlangen 91058, Germany*

[6] *Max Planck Institute for the Science of Light, Staudtstraße 2, Erlangen 91058, Germany*

[7] *Interdisciplinary Centre for Nanostructured Films, Cauerstr.3, Erlangen 91058, Germany*

(Received 20 March 2023; accepted 28 August 2023; published 16 October 2023)

No quantum system can be considered totally isolated from its environment. In most cases the interaction between the system of interest and the external degrees of freedom deeply changes its dynamics, as described by open quantum system theory. Nevertheless engineered environment can be turned into beneficial effects for some quantum information tasks. Here we demonstrate an optical simulator of a quantum system coupled to an arbitrary and reconfigurable environment built as a complex network of quantum interacting systems. We experimentally retrieve typical features of open quantum system dynamics like the spectral density and quantum non-Markovianity, by exploiting squeezing and entanglement correlation of a continuous-variable optical platform. This opens the way to the experimental tests of open quantum systems in reconfigurable environments that are relevant in, among others, quantum information, quantum thermodynamics, quantum transport, and quantum synchronization.

DOI: 10.1103/PRXQuantum.4.040310

I. INTRODUCTION

Quantum information technologies are nowadays getting to the regime where noisy intermediate-scale quantum (NISQ) systems [1] show quantum advantage when compared with classical equivalents [2–5].

Nevertheless, whatever the platform considered, both decoherence and losses are still obstacles that can be mitigated but not completely avoided [6,7], so any platform should be considered an open system. The theory of open quantum systems largely explored the role of the environment and showed that, when opportunely engineered, it can be promoted to be an ally of the open system [8–14].

Beyond quantum information platforms, the study of open quantum systems interacting with structured environment is essential for understanding biological systems [15–17], boosting quantum thermal machines [18,19] and machine-learning protocol [20], achieving collective phenomena such as dissipative phase transitions [21] or synchronization in the quantum realm [22,23] and explaining the emergence of the classical world from quantum constituents [24–26]. It is thus crucial to have experimental platforms to put to the test the variety of open quantum systems for different purposes. In this work we demonstrate an optical simulator of arbitrary quantum environments interacting with an open system. This can be understood as the ability to achieve engineered dissipation for quantum information science [27].

The fine-grained structure of the environment can be described in many cases as a network of quantum harmonic oscillators. We experimentally reproduce the dynamics of the open system coupled to networks whose interaction

*paul.renault@qc82.tech

†Current address: QC82, 7757 Baltimore Avenue, College Park, MD 20740, USA.

structure can take an arbitrary shape. More generally in this work we consider quantum complex networks, mimicking real-world ones [28], as examples of complex environments [29,30]. The role of the open system and of the network (environment) are played in the experiment by optical spectral modes interacting in a multimode nonlinear process pumped by a femtosecond laser.

We show that the quantum optical platform, by using squeezing and entanglement correlations as resources along with continuous-variable (CV) measurement [31,32], is able to reproduce two crucial features of the system-environment dynamics. The first one is the energy exchange and dissipation, characterized by the spectral density of the environmental coupling [33]. The second property is the quantum non-Markovianity (QNM) [34–38]. Specifically we test the QNM as introduced by Breuer *et al.* [36], consisting of a backflow of information from the environment to the system during the dynamics [39].

While there exists a number of experiments that have shown the ability to emulate open quantum systems and in particular to control Markovian–non-Markovian transition or dephasing effects [40–45], these have been mainly implemented via single or few qubits. Only preliminary experimental studies [46] of CV systems have been reported and without any control of the open system dynamics. Here we control the dynamics of an open system by interacting it with multipartite CV systems that emulate networks of quantum harmonic oscillators arranged in various tailored structures. We experimentally test the predicted correlation between the structures of the networks and their dissipative behavior, characterized by different spectral density features [47]. Additionally, we experimentally examine the correlation between the spectral density features and the potential backflow of information [33]. The measurements also validate two specific probing techniques for these quantities. The first technique involves monitoring the excitation number of an open system at multiple frequencies to probe the spectral density. The second technique probes the quantum non-Markovianity by monitoring the fidelity between two quantum states of the open system interacting with a specific environment. The agreement between the experimental results and the theoretically predicted features for various networks demonstrates the reliability of the experimental setup and the techniques, which can then be utilized to benchmark protocols with relevant [16] or unknown network structures within quantum environments.

Reservoir control and engineering are essential in quantum information tasks [27,48,49], which can be implemented in the optical setup supported by non-Gaussian features [50,51]. Also, the probed quantities, namely the spectral density and quantum non-Markovianity, are the key features to look at [52–58].

II. MAPPING OF THE OPEN QUANTUM SYSTEM INTO CV OPTICAL SYSTEMS

The open quantum system we emulate (S, also named the probe) is coupled to an environment (E), as shown in Fig. 1(a). S is a harmonic oscillator of frequency ω_s. The environment is modeled by an ensemble of N other harmonic oscillators coupled with each other via springlike interactions. The coupling strength between oscillators i and j is denoted as g_{ij}. Without loss of generality, we consider the case where the frequencies of the oscillators in E are the same, ω_0. We assume that S is coupled to only one node of the environmental network labeled l (see Fig. 1). The Hamiltonians of the network (H_E), of the system (H_S) and of their interaction (H_I) are [28,47]

$$H_E = \mathbf{p}^T \Delta_\omega \mathbf{p} + \mathbf{q}^T \sqrt{\Delta_\omega{}^{-1}}\, \mathbf{A} \sqrt{\Delta_\omega{}^{-1}}\, \mathbf{q}, \tag{1}$$

$$H_S = \omega_S \left(\frac{p_S^2}{2} + \frac{q_S^2}{2} \right), \tag{2}$$

$$H_I = k q_S q_l, \tag{3}$$

where $\mathbf{A}$ is a symmetric and real matrix of size (N) called the adjacency matrix of the environmental network, such that $A_{ij} = \delta_{ij}\omega_i^2/2 - (1 - \delta_{ij} g_{ij}/2)$, Δ_ω is a diagonal matrix whose all elements are ω_0, $\mathbf{q} = (q_1, \ldots q_N)^T$,

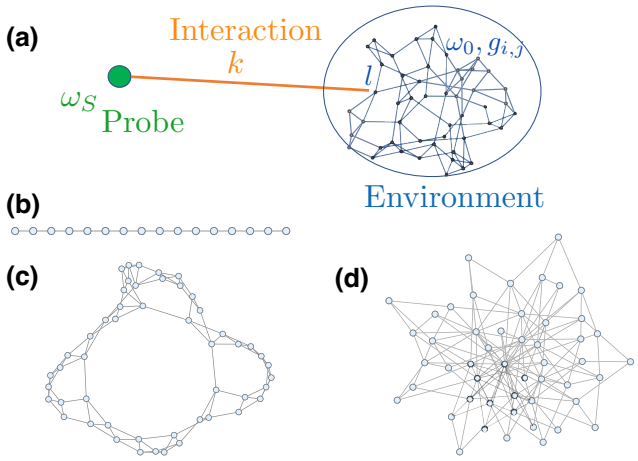

FIG. 1. Structure of the global system and environments. (a) Scheme of a global system where a probe (green) is attached to an environment network (blue) via a coupled strength k (orange). (b)–(d) Environment structures investigated in this work. (b) Linear structure used for the network 1, 2, and 3. These are networks of 16 nodes with periodic coupling strength. (c),(d) Structure that represents the environments called, respectively, network 4 and network 5 and both composed by $N = 50$ nodes. They are two instances of the Watts-Strogatz (WS) and Barabasi-Albert (BA) model as defined in complex networks theory [60,61]. The coupling strengths are constant within these two networks (the network parameters are given in Table I.

$\mathbf{p} = (p_1, \ldots p_N)^T$ and (p_S, q_S) stands for renormalized quadrature operators [59].

Hamiltonians in Eq. (3) are given with $\hbar = 1$, and $m = 1$. Also, in the rest of the paper numerical values of couplings and frequencies are specified relative to a fixed (arbitrary) frequency unit. This is because, on the one hand, any possible value and unit can be chosen in the simulations implemented via the optical system, and, on the other hand, the properties of the open system in the presence of different environments are driven by the ratio between involved frequency and coupling terms $\{\omega_S, \omega_0, g, k\}$ rather than their absolute value. We can easily derive the temporal dynamic of the full system, described by the evolution matrix $\mathscr{S}(t)$ such as

$$\mathbf{x}(t) = \mathscr{S}(t)\mathbf{x}(0), \tag{4}$$

where $\mathbf{x}(t) = (q_s, \mathbf{q}, p_s, \mathbf{p})$. More details about the derivation of $\mathscr{S}$ can be found in Ref. [28]. H_E, H_S, and H_I being quadratic Hamiltonians leading to Gaussian processes, at each time t the evolution matrix $\mathscr{S}(t)$ is symplectic. To study the energy transfer between the network and the system, some of the involved oscillators should be initialized in a nonzero energy state; such preparation can be included in the symplectic operation, $\mathscr{S}_{\text{eff}}(t) = \mathscr{S}(t)\mathscr{S}_{\text{in}}$, so that the global process can be written as

$$\begin{aligned}\mathbf{x}(t) &= \mathscr{S}_{\text{eff}}(t)\mathbf{x}_v(0) \\ &= \mathbf{R}_1(t)\Delta(t)\mathbf{R}_2(t)\mathbf{x}_v(0) = \mathbf{R}_1(t)\Delta(t)\mathbf{x}_v(0).\end{aligned} \tag{5}$$

The second line is the Bloch-Messiah decomposition of the symplectic transformation where $\mathbf{R}_1$ and $\mathbf{R}_2$ are orthogonal matrices, corresponding to linear optics operations (or more generally to basis change), while Δ is a diagonal matrix corresponding to squeezing operations [62]. As the initial state preparation is included in $\mathscr{S}_{\text{eff}}$, $\mathbf{x}_v(0)$ are quadratures of a collection of oscillators in the vacuum states and $\mathbf{R}_2$ can be discarded.

We can obtain the same transformation of Eq. (5) on quadratures of optical modes, using multimode squeezing (Δ) and mode basis change ($\mathbf{R}_1$). Experimentally, these can be implemented in optical parametric process pumped by an optical frequency comb and measured via ultrafast shaped homodyne detection [28,31,32]. We can thus emulate the evolution of the open quantum system at a time t by implementing the transformation $\mathbf{R}_1(t)\Delta(t)$ on optical modes of different optical spectrum that play the role of the harmonic oscillators composing the network and the system. Starting from a bunch of initial modes to which the squeezing operation $\Delta(t)$ is applied, the linear optics operation $\mathbf{R}_1(t)$ corresponds to a basis change that can be realized by measuring the quadratures $\mathbf{x}(t)$ via the appropriate local oscillator shape in homodyne detection [28,31]. This platform can simulate the dynamic of an open quantum system in environments with tunable spectral features, induced by environment. The environment can have any complex structure of correlations, as long as the number of optical modes that can be detected in the mode-selective homodyne—i.e., the number of addressable harmonic oscillators- is large enough. In the following we will show how our experimental system is able to simulate environments of different shape and size by recovering their specific features in the interaction with the open system. In particular we will recover the spectral density $J(\omega)$ [33], that reveals the energy flow between the system and the environment, and the quantum non-Markovian behaviors [36], i.e., an information backflow from the environment to the system.

In order to show the reconfigurability of our system we implement the networks shown in Fig. 1. We set three different linear networks of 16 nodes with different periodic coupling strength [33]. Then we set networks of 50 nodes derived from complex-network models like the Watts-Strogatz model, characterized by short average path lengths and high clustering [63], and the Barabasi-Albert model characterized by a power-law distribution of the degree [64].

III. SPECTRAL DENSITY FOR A GIVEN NETWORK

The reduced dynamic of the system in the presence of the environment can be derived by tracing out the environmental degrees of freedom from the evolution given by the total Hamiltonian $H_E + H_S + H_I$. In general, the evolution of the open system takes the form of a nonunitary master equation for the state, or an equivalent generalized Langevin equation for the position observable, [33,65–68]

TABLE I. Network characteristics. p_{WS} and κ are, respectively, the rewiring probability in the Watts Strogatz model and the connection parameter in the Barabasi-Albert model.

Network	ω_0	N	Type	k	g
1	0.25	16	linear	0.01	periodic: 0.1; 0.05; 0.1 ...
2	0.25	16	linear	0.01	periodic: 0.1; 0.1; 0.05; 0.1 ...
3	0.25	16	linear	0.01	periodic: 0.1; 0.05; 0.025; 0.1 ...
4	0.25	50	Watts-Strogatz: $p_{\text{WS}} = 0.1$	0.02	0.08
5	0.25	50	Barabasi-Albert: $\kappa = 2$	0.004	0.02

such as,

$$\ddot{q_S} + \tilde{\omega}_S^2 q_S + \int_0^t d\tau \gamma(t-\tau)\dot{q_S} = \xi(t), \tag{6}$$

where $\tilde{\omega}_S$ is a renormalized system frequency and $\xi(t)$ is Langevin forcing of the system. The dissipation and memory effect of the system are featured by the damping kernel $\gamma(t)$. This can be equivalently characterized via the spectral density defined as

$$J(\omega_S) = \omega_S \int_0^{t_{\max}} dt \gamma(t) \cos(\omega_S t). \tag{7}$$

The value of the spectral density at a given frequency ω_S shows the strength of the energy flow between the system and the environment, e.g., its damping rate. Specific network structures of the environment are characterized by different shapes of $J(\omega_S)$ that can be easily recovered by calculating the evolution of the system plus the environment via the total Hamiltonian in Eq. (3) and getting $\gamma(t)$ from the reduced dynamics of the system. It should be noted that $J(\omega_S)$ in Eq. (7) is normally defined with $t_{\max} = \infty$ but as here we are dealing with finite environments we set a finite $t_{\max}$, which can be considered as the time the open system interacts with all the elements of the networks before the revival dynamics arises due to the finite size effects of the environment (see Sec. VI A).

For unknown network structures, the shape of $J(\omega_S)$ can be recovered by probing the excitation number of the system S that interacts with the environment [28,33,47] at different frequencies ω_S [see Eq. (9) in Sec. VI A]. This is the approach we follow in the experimental simulation: given all the network parameters, the experimental setup composed by different optical modes can implement the quadrature evolution $\mathbf{x}(t)$ of the network plus the system in Eq. (5). We get the value of $J(\omega_S)$ by monitoring the excitation number $\langle \hat{n_S} \rangle$, that can be recovered from homodyne measurements of $\langle \hat{q_S}^2 \rangle$ and $\langle \hat{p_S}^2 \rangle$ and we compare the results with the expected theoretical shape. The protocol is shown in Fig. 2. The experimental data in Fig. 3 are obtained from homodyne measurements of the mode corresponding to (S) having interacted with (E) until $t_{\max}$. Each dot is the value of $J(\omega_S)$ recovered when the environment interacts with the system at a specific frequency ω_S. This corresponds to a given measurement setting, i.e., to a given basis change $\mathbf{R}_1(t_{\max}, \omega_S)$ in Eq. (5), and in particular to a given local oscillator (LO) spectrum in the homodyne measurement, set by the spatial light modulator (SLM) mask. One dot on each curve is the average of 20 measurements and the error bars are obtained from the standard deviation. The theoretical curves are calculated from Eq. (7) given the parameters of the networks shown in Fig. 1 (see Sec. VI A). Except for some noise due to the instabilities of the experimental system, the experimental data shown in Fig. 3 match the shapes of the theoretical curves for all linear and complex environments. In the network picture, squeezing determines the absolute strength of couplings. As mentioned earlier, the resolved features, on the other hand, depend solely on the relative strengths of frequencies and coupling terms ω_S, ω_0, g, k. The measured quantities,

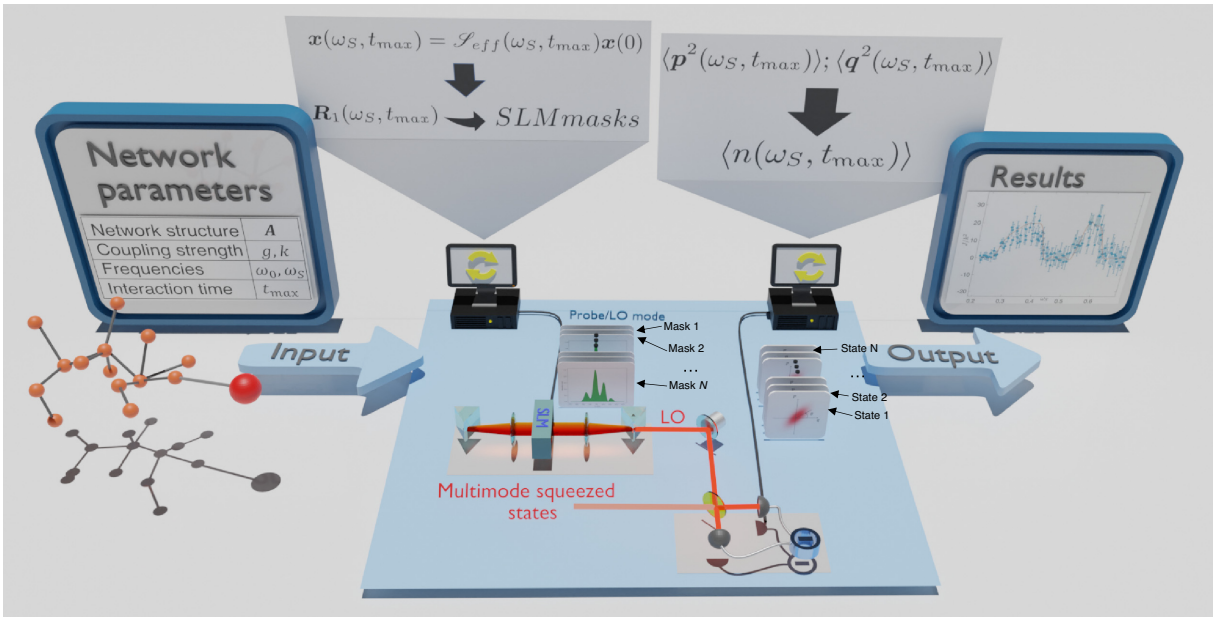

FIG. 2. Protocol for the recovery of the spectral density function for a given environment. The parameters of a given network are used to calculate the quadrature dynamics of the system S for different frequencies ω_S while the decomposition of such an evolution gives the measurement setting, $\mathbf{R}_1(\omega_S)$ is tied to a specific mask for the spatial light modulator (SLM) in the shaping of the local oscillator (LO). Measurement of $\langle \hat{q}_S^2 \rangle$ and $\langle \hat{p}_S^2 \rangle$ via the quadrature statistics are associated to the $\langle \hat{n}_S \rangle$ value and then to $J(\omega_S)$.

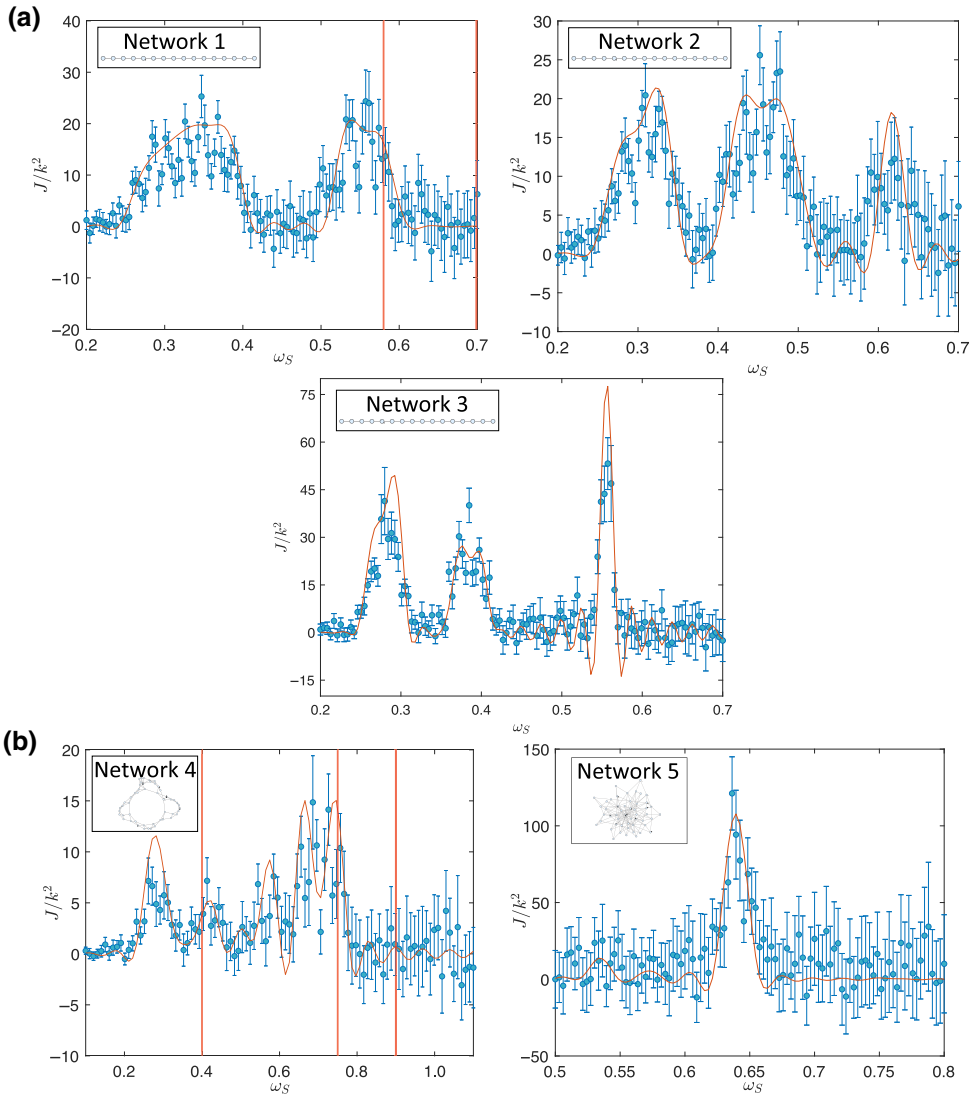

FIG. 3. Spectral density measurements. Spectral density as a function of the frequency ω_s when the environment has a linear structure (a) or a complex structure (b). Orange lines, theoretical calculation; blue dots, experimental values recovered by probing the optical mode simulating the open system. Red vertical lines show the probe frequencies of network 1 and 4 for which QNM is investigated.

however, are proportional to quadrature variances. Therefore, the maximum values are directly proportional to the achievable experimental squeezing values, which should exceed the experimental noise. The amplitude of small discrepancies and the size of the error bars represent the limits of the smallest features that can be detected in the spectral density using the current experiment. Getting better system stability and noise filtering in the detection stage are attainable through technical improvements. In each plot, we observe the emergence of several peaks at specific frequencies. These peaks indicate that, at those frequencies, the open system dissipates energy into the environment. The resolution of the peak is determined by the choice of the interaction time [28].

IV. QUANTUM NON-MARKOVIANITY

In addition we further demonstrate the versatility of our platform by experimentally observing the connection between NM and local shape of $J(\omega)$, previously predicted theoretically [33]. In this work we use the definition of quantum non-Marknovianity (QNM) introduced by Breuer *et al*. in Ref. [36], where the memory effect in the system is associated to a backflow of information from E to S. A Markovian process continuously tends to reduce the distinguishability between any two quantum states of a given system, in a non-Markovian behavior it tends to increase, so that the flow of information about such distinguishability is reversed from the environment to the system. The original definition of QNM based on trace distance between the states can be expressed, in the case of Gaussian states, via the fidelity as proposed in Refs. [36,69]. Therefore, we use the following QNM witness:

$$\mathcal{N} = \max_{\rho_1,\rho_2} \int_{\frac{\partial F}{\partial t}<0} dt\Big(-\frac{\partial F}{\partial t}\Big), \tag{8}$$

where (ρ_1, ρ_2) is a pair of initial states of S at $t = 0$ and F their fidelity defined throughout the interaction duration. In fact, a quantum process is considered non-Markovian

when the distance between the states ρ_1 and ρ_2 increases over a nonzero time interval. This corresponds to a reduction in the fidelity during that interval. The decreasing tendency of the fidelity is then interpreted as an increasing distinguishability and, consequently, a backflow of information from the environment into the system.

Experimentally only a finite set of quantum states can be accessed, we have then chosen the two experimentally accessible states ρ_1, ρ_2 that minimize the fidelity at $t = 0$ (see Appendix B), in order to have the maximal sensitivity in the QNM witness $\mathcal{N}$. Such states are two vacuum squeezed states that are squeezed along two orthogonal directions (see Secs. V and VI B).

The quantum non-Markovianity can be associated to specific structures of the spectral density [33], in particular, it has been shown that maximal values of $\mathcal{N}$ are reached at the edges of a band gap in the spectral density, where the band gap is a region where $J(\omega_S)$ is close to zero. In this protocol we focus on some given values of the probe frequency where the spectral density of specific networks (linear and WS) have particular features: large values, or being within or at the edge of the gap. For each time t the protocol is performed for two different input states ρ_{1sq} and $\rho_{2sq\perp}$, in order to measure their fidelity. The first state ρ_{1sq} has squeezing of -1.8 dB along the q quadrature and antisqueezing of $+2.9$ dB, and the second $\rho_{2sq\perp}$ has squeezing of -1.3 dB along the p quadrature and antisqueezing of $+2.4$ dB. The fidelity between the two states is calculated via the covariance matrix of the two recovered via the measurement of $\langle \hat{q}_S^2 \rangle$ and $\langle \hat{p}_S^2 \rangle$.

Figure 4 shows the fidelity measurement as a function of time t for the linear periodic network called network 1 and the Watts-Strogatz network at given values of frequency ω_S. For both environments we can observe a backflow of the information in the system for some of the monitored frequencies of the probe. When the environment takes the form of network 1, the system is non-Markovian for $\omega_S = 0.58$, at the edge of the gap [33], while no information exchange is perceived between the system and the environment for $\omega_S = 0.70$. At such frequency, the dynamics of the system can be interpreted as unitary, as shown by a value of $J(\omega_S)$ close to 0 in Fig. 3(A). In the case of the Watts-Strogatz network, non-Markovianity is observed for $\omega_S = 0.4$ and $\omega_S = 0.75$ with a larger information backflow for the latter, while no information exchange is noticeable at $\omega_S = 0.9$. In order not to overestimate the witness value because of high-frequency fluctuations in the experimental data, the derivative of Eq. (8) is evaluated on averaged curves (solid lines in Fig. 4). The obtained values of $\mathcal{N}$ are gathered in Table II.

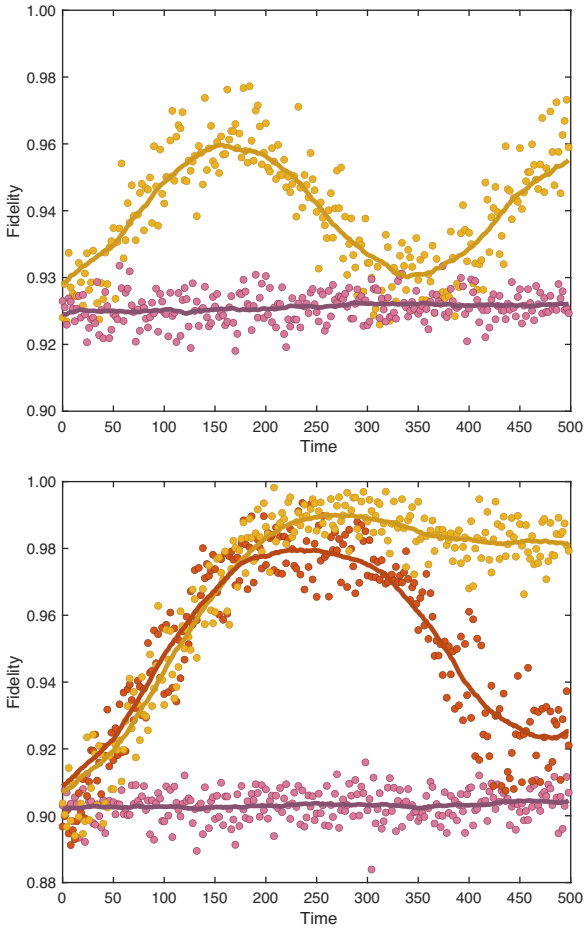

FIG. 4. Fidelity as a function of the time parameter for several probe frequencies. (Top) The environment takes the form of network 1 and pink and yellow dots are, respectively, for $\omega_S = 0.7$ and $\omega_S = 0.58$. (Bottom) The environment takes the form of the Watts-Strogatz network, pink dots are measured for $\omega_S = 0.9$, red dots for $\omega_S = 0.75$, and the yellow dots for $\omega_S = 0.4$. Solid lines are obtained via averaging over 50 points. Strong initial increase of fidelity corresponds to the edges of $J(\omega)$, see red vertical lines of Fig. 3.

V. THE EXPERIMENTAL SETUP

A general scheme of the experiment is shown in Fig. 5. The main goal is to produce highly multimode nonclassical light. Frequency-doubled pulses from a Ti:sapphire laser are propagated in an OPO cavity with round-trip time matched to the pump-pulse train-cycle time. The nonlinear crystal inside the cavity is a BiBO crystal of length 0.2 mm. The repetition rate of the pulse train is 75 MHz and pulses have a duration of about 100 fs. Correlations

TABLE II. Non-Markovian witnesses for network 1 and 4.

ω_S	$\mathcal{N}$ of network 1	$\mathcal{N}$ of WS network
0.4	–	0.013
0.58	0.041	–
0.7	0.012	–
0.75	–	0.06
0.9	–	0.012

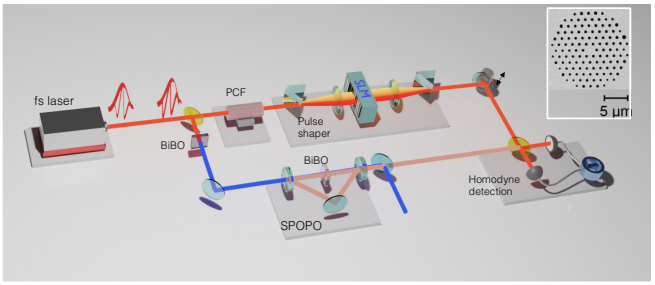

FIG. 5. Scheme of the experimental setup. The beam from the femtosecond laser source is divided in two paths: the first one to produce multimode squeezed light (second-harmonic generation + SPOPO cavity) and the second one to spectrally shape the local oscillator (PCF + pulse shaper). The two beams are then recombined for the homodyne detection. Inset: electron micrograph of the end face of the PCF.

appear among many spectral modes of the frequency comb of the down-converted light, giving rise to a squeezed vacuum state at 795-nm central wavelength with a highly multimode structure [31,32]. This multimode squeezing structure can be measured via a spectrally resolved homodyne detection. A pulse shaper, located upstream, enables the spectral mode of the local oscillator to be set in the homodyne detection. We find that the squeezed spectral modes are described by a set of Hermite-Gaussian functions. The first one of the series is a Gaussian function with FWHM of around 6.5 nm. The quadratures' evolution of the involved optical modes in the parametric process is described by an equation of the same form of Eq. (5). The harmonic oscillators initially in a vacuum state and whose quadratures are squeezed as $\Delta(t)\mathbf{x}(0)$ are, in the actual setup, the squeezed modes. The quadratures $\mathbf{x}(t) = \mathbf{R}_1(t)\Delta(t)\mathbf{x}(0)$ are the ones accessed via homodyne detection. The transformation $\mathbf{R}_1(t)$ describes the basis change from the modes with Hermite-Gauss spectral shapes to the measured modes [31,32,70]. In order to exactly match the evolution of the multimode optical system with the one of the network plus the probe, we have to set both the squeezing values in $\Delta(t)$ and the detected pulse shapes given by $\mathbf{R}_1(t)$. In the present experiment, numerical analysis showed that the probing of $J(\omega_S)$ and $\mathcal{N}$ are not very sensitive to changes in the squeezing values in $\Delta(t)$. In these protocols the numbers and values of nonzero diagonal terms in Δ set the number of oscillators that are initially in a not-vacuum state and the value of their excitation numbers. Interactions between the oscillators and their evolution can be established via $\mathbf{R}_1(t)$. Thus only $\mathbf{R}_1(t)$ is modified accordingly to the dynamics we have to simulate. In both protocols (probing of spectral density and quantum non-Markovianity) we follow the spread of energy and information from few initially populated harmonic oscillators to a large number of harmonic oscillators in the networks. So if the number of the harmonic oscillators that can be initially set in a not-vacuum state is limited by the number of produced squeezed modes, the number of harmonic oscillators that can be reached by some excitation (i.e., the number of the total oscillators in the networks) is limited by the number of spectral modes we can measure, as this is what limit the size of the matrix $\mathbf{R}_1(t)$. A larger number of spectral modes to measure means a larger spectrum to be shaped for the local oscillator field. Ultimately, the number of simulated harmonic oscillators depends on the capability of the pulse shaper, which is limited by the optical complexity [71] and the spectral width of the field that is used as the local oscillator. In order not to be limited by the latter, the local oscillator, that is derived from the main laser source, is broadened with a 2-cm-long all-normal dispersion photonic crystal fiber (PCF) before entering the pulse shaper stage. In such a fiber, the broadening mechanism relies only on self-phase modulation, which is known to be low noise [72]. If needed in future experiments and protocols, $\Delta(t)$ can be opportunely controlled via the shaping of the pump in the parametric process [73].

VI. PROTOCOLS

A. Spectral density measurement

The protocol is based on the bosonic resonator network mapping established by Nokkala *et al.* [28]. In Table III the equivalent items involved in the mapping are gathered to emulate the network of the bosonic oscillator.

As shown in Fig. 2, the protocol is carried out in two stages: first, basis change and accordingly the mask characteristics setting the probe measurement are computed by a Wolfram MATHEMATICA code and second, the variances $\langle \hat{q}_S^2 \rangle$ and $\langle \hat{p}_S^2 \rangle$ are measured. The process is as follows:

(i) Interaction time $t_{\max}$, environment structure, coupling strength g and k, and the frequency ω_0 are set and entered in the code. At first, the damping kernel $\gamma(t)$ is numerically calculated and then we selected as $t_{\max}$ a value where the resulting solution is flat and close to 0. The γ computation for the considered environments are in Appendix A.

TABLE III. Mapping of experimental implementation for the quantum network for the open quantum system.

Network component	Quantum network	Experimental implementation
Node	Quantum harmonic oscillator	Optical mode
Link	Coupling strength	Entanglement or basis change
Addressing a node	Local measurement	Pulse shaping and projective measurement

For sufficiently short times the system cannot resolve the different frequencies of the network, making the spectral density a continuous function of frequency in this regime, as seen in Fig. 3. For some networks the spectral density additionally assumes a constant form for a transient where the shape is not sensitive to small differences in interaction time. The set interaction times for each network are $t_{\max,1} = t_{\max,2} = t_{\max,3} = 150$, $t_{\max,4} = 90$, and $t_{\max,5} = 250$.

(ii) A set of matrices $\mathscr{S}_{\text{eff}}(t_{\max}, \omega_s)$ is evaluated for 120 values of ω_s in the range $\{0.2, 0.7\}$ for networks 1, 2, and 3. Then 100 matrices are also computed in the ranges $\{0.1, 1.1\}$ and $\{0.5, 0.8\}$ for, respectively, networks 4 and 5. The matrices $\mathbf{R}_1(t_{\max}, \omega_s)$ and $\Delta(t_{\max}, \omega_s)$ are obtained from the Bloch Messiah decomposition.

(iii) From $\mathbf{R}_1(t_{\max}, \omega_s)$ we can derive the spectral mode corresponding to the system and probe of frequency ω_s having interacted with the network for the time $t_{\max}$. The corresponding optical spectrum of the local oscillator is shaped via the SLM masks. The average values $\langle \hat{q}_S^2 \rangle$ and $\langle \hat{p}_S^2 \rangle$ are obtained via homodyne detection.

(iv) The average photon number $\langle n_S(t_{\max}) \rangle$ of the system is derived so that we can get $J(\omega_s)$ from the following equation: [28]

$$J(\omega_s) = \frac{\omega_s}{t_{\max}} \ln\left(\frac{N(\omega_s) - \langle n_S(0) \rangle}{N(\omega_s) - \langle n_S(t_{\max}) \rangle}\right), \quad (9)$$

where $N(\omega_s) = \left(e^{\omega_S/T} - 1\right)^{-1}$ is the thermal average boson number with T being the temperature of the environment.

B. Quantum non-Markovianity

Although the emulated total system dynamic remains unchanged, the way to highlight QNM is slightly different than the way to recover the spectral density function. The variable choice is the first way to distinguish them since the interaction time is varying for the QNM witness measurement instead of the probe frequency for the spectral density. The second distinction is within the number of modes, which are measured to get one data point: two SLM masks are generated in the case of the fidelity against one mask for one data point for the spectral density. Hence the protocol for fidelity measurement is as follows:

(i) Environment structure, coupling strength g and k, the frequency ω_0 and the probe frequency ω_s are set and entered in the code.

(ii) A set of matrices $\mathscr{S}_{\text{eff}}(t, \omega_s)$ is evaluated for 251 values of t in the range $\{0, 500\}$. The same set is applied to two different input states for the probe and system oscillator, ρ_{1sq} and $\rho_{2sq\perp}$ consisting in two vacuum states squeezed along two orthogonal directions. The two are naturally encoded in the first two modes HG_0, HG_1 of the Hermite-Gauss series that diagonalize the parametric down-conversion Hamiltonian, $\rho_{\text{HG}_0}(0) = \rho_{1sq}$; $\rho_{\text{HG}_1}(0) = \rho_{2sq\perp}$.

(iii) The set of SLM masks corresponding to the temporal evolution of the two initially squeezed oscillators are evaluated.

(iv) Homodyne measurements are used for the evaluation of the states $\rho_{\text{HG}_0}(t)$ and $\rho_{\text{HG}_1}(t)$ at time t and their fidelity.

VII. CONCLUSION

In summary, we have experimentally demonstrated the simulation of an open system coupled to complex network environments of different shape. Any network shape can be engineered and probed in the actual platform. In particular, we have shown probing techniques for the spectral density of the environmental coupling and of the quantum non-Markovianity. Our platform is the first experimental setup where continuous-variable open systems with engineered environment are tested. It goes beyond the few-qubits implementation by controlling a multipartite system with up to 50 components. The environment and system size can be increased in future experiments by considering both spectral and time multiplexing [74], moreover non-Gaussian interaction can be added [50,51]. Hence, implementing a non-Gaussian state in either the system or the environment nodes will open perspective for a quantum simulator of open quantum system that cannot be simulated by a classical computer. Applications are relevant in the context of quantum information technologies since for any spectral density $J(\omega)$, a linear network as environment may be found, which reproduces it once coupled to the probe. Several algorithms have been developed in that direction [75–77]. Dissipation phenomena in energy transfer and, in particular, vibronic dynamic can be mapped via the demonstrated experimental apparatus [15–17] opening the way to the test of artificial light-harvesting architecture. Moreover, we can test engineered environment to enhance quantum thermal machines [18,19]. Finally, we can explore different probing schemes like multiple harmonic oscillators (measured modes) coupled with different partitioning of the environment, via weak or strong interaction. We can then test paradigmatic collective phenomena, like quantum phase transitions and quantum synchronization [21–23] and the emergence of classical world from the quantum one as the effect of the interaction with a structured environment [24–26].

ACKNOWLEDGMENTS

This work was supported by the European Research Council under the Consolidator Grant COQCOoN (Grant

No. 820079). S.M. acknowledges financial support from the Academy of Finland via the Centre of Excellence program (Projects No. 336810 and No. 336814). J.N. acknowledges financial support from the Turku Collegium for Science, Medicine and Technology as well as the Academy of Finland under Project No. 348854. R.Z. acknowledges funding from the Spanish State Research Agency, through the María de Maeztu Project CEX2021-001164-M and the QUARESC Project PID2019-109094GB-C21 (AEI/10.13039/501100011033), and CAIB QUAREC Project (PRD2018/47).

APPENDIX A: DAMPING KERNEL SIMULATION

Regarding the determination of the spectral density J associated to a given environment, the interaction time, $t_{\max}$ in the article, must be set before the measurement. Some restrictions enumerated in the main text apply on this choice.

For each investigated network in the paper, the γ evolution is analytically simulated. The results are shown in Fig. 6. $t_{\max}$ is set among the time range $[0, 500]$ where γ reaches a region as flat as possible. Let us notice that for the linear networks the interval where can be set $t_{\max}$ is more easily distinguishable than for the complex networks.

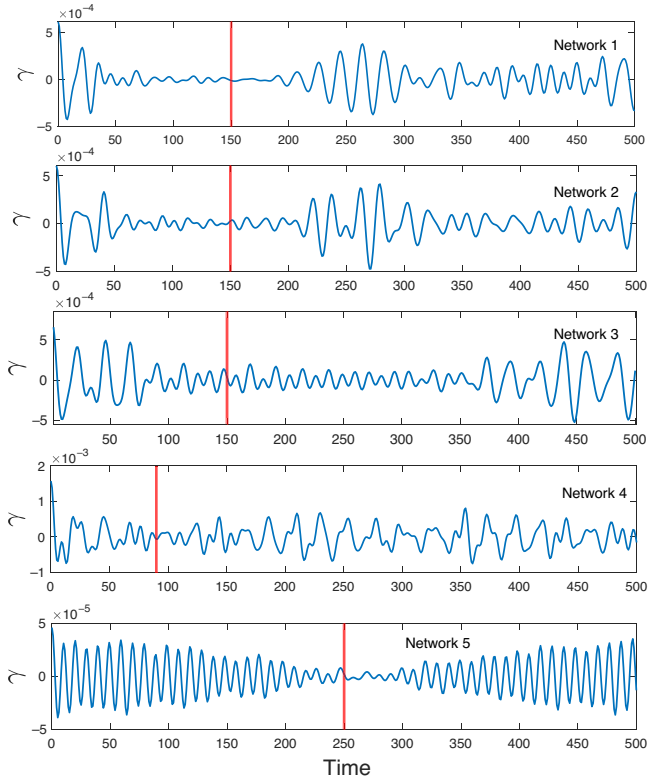

FIG. 6. Analytical simulation of damping kernel as a function of time for all networks. For each network implemented as the environment of the probe, the resulting damping kernel exhibits the same shape: first, a decay of the oscillations' amplitude is observed until reaching then a more or less long plateau where it is set $t_{\max}$. The red lines show the position of $t_{\max}$ selected for the simulation of the different total system dynamics.

APPENDIX B: WITNESSING NON-MARKOVIANITY WITH PURE SQUEEZED STATES

The used witness $\mathcal{N}$ of quantum non-Markovianity (QNM), specified in Sec. 2.3 of the main paper, involves a maximization over pairs of distinct initial states. Experimental quantification will naturally limit the possible pairs to experimentally accessible states, such as pure squeezed states characterized by the magnitude r_i and phase φ_i of squeezing where the index $i \in \{1, 2\}$ indicates the two states.

Here plausibility is provided for the following claims: non-Markovianity is witnessed independently of the initial phase difference $\varphi_0 := \varphi_1 - \varphi_2$; squeezing opposite quadratures, as we have done, can be expected to give the highest value for $\mathcal{N}$ in this set of states. In particular, if the open system dynamics is found to be (non-)Markovian for one choice of φ_0 it will be found (non-)Markovian for all values $\varphi_0 \neq 0$; only the numerical value of $\mathcal{N}$ will change.

The key argument is that the choice of φ_0 maximizing distinguishability at $t = 0$ maximizes it also for any time $t > 0$ whereas the qualitative behavior is independent of φ_0. As will be seen, this is a consequence of the following points, suggested both by intuition and numerical simulations:

(1) the phase difference remains nearly constant: $\varphi(t) \approx \varphi_0$;
(2) $r_i(t)$ is nearly independent of φ_i;
(3) qualitative behavior of $r_i(t)$ is not sensitive to $r_i(0)$.

We start from the fidelity F between the two states. It reads

$$F = \frac{2}{\sqrt{2(1 + \cosh 2r_1 \cosh 2r_2 - \cos\varphi_0 \sinh 2r_1 \sinh 2r_2)}}. \tag{B1}$$

As anticipated only the relative phase matters. We turn our attention to $F(t)$. Because of point (1) we may substitute $\varphi(t)$ with φ_0. Then the squeezing parameters are the only source of nonmonotonicity.

$$F(t) \approx \frac{2}{\sqrt{2(1 + \cosh 2r_1(t) \cosh 2r_2(t) - \cos\varphi_0 \sinh 2r_1(t) \sinh 2r_2(t))}}. \tag{B2}$$

We consider two limiting cases: identical phase $\varphi_0 = 0$ and opposite phase $\varphi_0 = \pi$. Because of point (2) the resulting expressions can be directly compared. We get for the two, respectively,

$$F(t) \approx \frac{2}{\sqrt{\cosh^2(r_1(t) - r_2(t))}}, \tag{B3}$$

$$F(t) \approx \frac{2}{\sqrt{\cosh^2(r_1(t) + r_2(t))}}. \tag{B4}$$

As expected, these are the maximal and minimal values of fidelity, respectively, in the interval $\varphi_0 \in [0, \pi]$ because there $F(t)$ is monotonically decreasing. This follows from the non-negativity of the hyperbolic functions and continuity in $\cos\varphi_0$, which is monotonous in $[0, \pi]$. Given point (3), full contribution of nonmonotonicity from both squeezings is achieved only in the latter case and, therefore, $\mathcal{N}$ is maximized when $\varphi_0 = \pi$.

In the special case $r_1 = r_2 := r$ point (3) becomes unnecessary. Here fidelity in general and in the case $\varphi_0 = \pi$, respectively, simplifies to

$$F(t) \approx \frac{2}{\sqrt{\cosh(4r(t))(1 - \cos\varphi_0) + \cos\varphi_0 + 3}}, \tag{B5}$$

$$F(t) \approx \mathrm{sech} 2r(t). \tag{B6}$$

There are caveats. First of all, this is clearly not a proof but rather justifies why our choice for the initial states and the interpretation of the results are reasonable. Second, the equations above implicitly assume pure states. Since we have used a weak coupling and pure state for the network purity can be expected to remain high for the considered times and fidelity should behave as above. This has been checked with numerical simulations.

[1] J. Preskill, Quantum computing in the NISQ era and beyond, Quantum **2**, 79 (2018).

[2] H.-S. Zhong *et al.*, Quantum computational advantage using photons, Science **370**, 1460 (2020).

[3] F. Arute *et al.*, Quantum supremacy using a programmable superconducting processor, Nature **574**, 505 (2019).

[4] Y. Wu *et al.*, Strong quantum computational advantage using a superconducting quantum processor, Phys. Rev. Lett. **127**, 180501 (2021).

[5] L. S. Madsen, F. Laudenbach, M. F. Askarani, F. Rortais, T. Vincent, J. F. Bulmer, F. M. Miatto, L. Neuhaus, L. G. Helt, M. J. Collins, Adriana E. Lita, Thomas Gerrits, Sae Woo Nam, Varun D. Vaidya, Matteo Menotti, Ish Dhand, Zachary Vernon, Nicolás Quesada, and Jonathan Lavoie, Quantum computational advantage with a programmable photonic processor, Nature **606**, 75 (2022).

[6] C. Berdou, A. Murani, U. Reglade, W. Smith, M. Villiers, J. Palomo, M. Rosticher, A. Denis, P. Morfin, and M. Delbecq *et al.*, One hundred second bit-flip time in a two-photon dissipative oscillator, arXiv preprint arXiv:2204.09128 (2022).

[7] R. Lescanne, M. Villiers, T. Peronnin, A. Sarlette, M. Delbecq, B. Huard, T. Kontos, M. Mirrahimi, and Z. Leghtas, Exponential suppression of bit-flips in a qubit encoded in an oscillator, Nat. Phys. **16**, 509 (2020).

[8] M. J. Biercuk, H. Uys, A. P. VanDevender, N. Shiga, W. M. Itano, and J. J. Bollinger, Optimized dynamical decoupling in a model quantum memory, Nature **458**, 996 (2009).

[9] F. Verstraete, M. M. Wolf, and J. Ignacio Cirac, Quantum computation and quantum-state engineering driven by dissipation, Nat. Phys. **5**, 633 (2009).

[10] J. T. Barreiro, P. Schindler, O. Gühne, T. Monz, M. Chwalla, C. F. Roos, M. Hennrich, and R. Blatt, Experimental multiparticle entanglement dynamics induced by decoherence, Nat. Phys. **6**, 943 (2010).

[11] V. V. Albert, B. Bradlyn, M. Fraas, and L. Jiang, Geometry and response of Lindbladians, Phys. Rev. X **6**, 041031 (2016).

[12] C. P. Koch, Controlling open quantum systems: Tools, achievements, and limitations, J. Phys.: Condens. Matter **28**, 213001 (2016).

[13] B.-H. Liu, X.-M. Hu, Y.-F. Huang, C.-F. Li, G.-C. Guo, A. Karlsson, E.-M. Laine, S. Maniscalco, C. Macchiavello, and J. Piilo, Efficient superdense coding in the presence of non-Markovian noise, EPL (Europhysics Letters) **114**, 10005 (2016).

[14] Z.-D. Liu, O. Siltanen, T. Kuusela, R.-H. Miao, C.-X. Ning, C.-F. Li, G.-C. Guo, and J. Piilo, Efficient quantum teleportation under noise with hybrid entanglement and reverse decoherence, arXiv preprint arXiv:2210.14935 (2022).

[15] A. Mattioni, F. Caycedo-Soler, S. F. Huelga, and M. B. Plenio, Design principles for long-range energy transfer at room temperature, Phys. Rev. X **11**, 041003 (2021).

[16] F. Caycedo-Soler, A. Mattioni, J. Lim, T. Renger, S. Huelga, and M. Plenio, Exact simulation of pigment-protein complexes unveils vibronic renormalization of electronic parameters in ultrafast spectroscopy, Nat. Commun. **13**, 1 (2022).

[17] A. Nüßeler, D. Tamascelli, A. Smirne, J. Lim, S. F. Huelga, and M. B. Plenio, Fingerprint and universal Markovian closure of structured bosonic environments, Phys. Rev. Lett. **129**, 140604 (2022).

[18] G. Manzano, G.-L. Giorgi, R. Fazio, and R. Zambrini, Boosting the performance of small autonomous refrigerators via common environmental effects, New J. Phys. **21**, 123026 (2019).

[19] M. Kloc, K. Meier, K. Hadjikyriakos, and G. Schaller, Superradiant Many-qubit absorption refrigerator, Phys. Rev. Appl. **16**, 044061 (2021).

[20] A. Sannia, R. Martínez-Peña, M. C. Soriano, G. L. Giorgi, and R. Zambrini, Dissipation as a resource for quantum reservoir computing, arXiv preprint arXiv:2212.12078 (2022).

[21] F. Minganti, A. Biella, N. Bartolo, and C. Ciuti, Spectral theory of Liouvillians for dissipative phase transitions, Phys. Rev. A **98**, 042118 (2018).

[22] G. Manzano, F. Galve, G. L. Giorgi, E. Hernández-García, and R. Zambrini, Synchronization, quantum correlations and entanglement in oscillator networks, Sci. Rep. **3**, 1439 (2013).

[23] A. Cabot, G. L. Giorgi, F. Galve, and R. Zambrini, Quantum synchronization in dimer atomic lattices, Phys. Rev. Lett. **123**, 023604 (2019).

[24] F. Galve, R. Zambrini, and S. Maniscalco, Non-Markovianity hinders quantum Darwinism, Sci. Rep. **6**, 19607 (2016).

[25] T. P. Le and A. Olaya-Castro, Strong quantum Darwinism and strong independence are equivalent to spectrum broadcast structure, Phys. Rev. Lett. **122**, 010403 (2019).

[26] C. Foti, T. Heinosaari, S. Maniscalco, and P. Verrucchi, Whenever a quantum environment emerges as a classical system, it behaves like a measuring apparatus, Quantum **3**, 179 (2019).

[27] P. M. Harrington, E. J. Mueller, and K. W. Murch, Engineered dissipation for quantum information science, Nat. Rev. Phys. **4**, 660 (2022).

[28] J. Nokkala, F. Arzani, F. Galve, R. Zambrini, S. Maniscalco, J. Piilo, N. Treps, and V. Parigi, Reconfigurable optical implementation of quantum complex networks, New J. Phys. **20**, 053024 (2018).

[29] A. Asenjo-Garcia, M. Moreno-Cardoner, A. Albrecht, H. Kimble, and D. E. Chang, Exponential improvement in photon storage fidelities using subradiance and "selective radiance" in atomic arrays, Phys. Rev. X **7**, 031024 (2017).

[30] M. Bello, G. Platero, J. I. Cirac, and A. González-Tudela, Unconventional quantum optics in topological waveguide QED, Sci. Adv. **5**, eaaw0297 (2019).

[31] Y. Cai, J. Roslund, G. Ferrini, F. Arzani, X. Xu, C. Fabre, and N. Treps, Multimode entanglement in reconfigurable graph states using optical frequency combs, Nat. Commun. **8**, 1 (2017).

[32] J. Roslund, R. M. De Araujo, S. Jiang, C. Fabre, and N. Treps, Wavelength-multiplexed quantum networks with ultrafast frequency combs, Nat. Photonics **8**, 109 (2014).

[33] R. Vasile, F. Galve, and R. Zambrini, Spectral origin of non-markovian open-system dynamics: A finite harmonic model without approximations, Phys. Rev. A **89**, 022109 (2014).

[34] Á. Rivas, S. F. Huelga, and M. B. Plenio, Entanglement and non-Markovianity of quantum evolutions, Phys. Rev. Lett. **105**, 050403 (2010).

[35] Á. Rivas, S. F. Huelga, and M. B. Plenio, Quantum non-Markovianity: Characterization, quantification and detection, Rep. Prog. Phys. **77**, 094001 (2014).

[36] H.-P. Breuer, E.-M. Laine, and J. Piilo, Measure for the degree of non-Markovian behavior of quantum processes in open systems, Phys. Rev. Lett. **103**, 210401 (2009).

[37] L. Li, M. J. Hall, and H. M. Wiseman, Concepts of quantum non-Markovianity: A hierarchy, Phys. Rep. **759**, 1 (2018).

[38] E.-M. Laine, J. Piilo, and H.-P. Breuer, Measure for the non-Markovianity of quantum processes, Phys. Rev. A **81**, 062115 (2010).

[39] H.-P. Breuer, E.-M. Laine, J. Piilo, and B. Vacchini, Colloquium: Non-Markovian dynamics in open quantum systems, Rev. Mod. Phys. **88**, 021002 (2016).

[40] B.-H. Liu, L. Li, Y.-F. Huang, C.-F. Li, G.-C. Guo, E.-M. Laine, H.-P. Breuer, and J. Piilo, Experimental control of the transition from Markovian to non-Markovian dynamics of open quantum systems, Nat. Phys. **7**, 931 (2011).

[41] J. T. Barreiro, M. Müller, P. Schindler, D. Nigg, T. Monz, M. Chwalla, M. Hennrich, C. F. Roos, P. Zoller, and R. Blatt, An open-system quantum simulator with trapped ions, Nature **470**, 486 (2011).

[42] S. Cialdi, M. A. C. Rossi, C. Benedetti, B. Vacchini, D. Tamascelli, S. Olivares, and M. G. A. Paris, All-optical quantum simulator of qubit noisy channels, Appl. Phys. Lett. **110**, 081107 (2017).

[43] S. Yu, Y.-T. Wang, Z.-J. Ke, W. Liu, Y. Meng, Z.-P. Li, W.-H. Zhang, G. Chen, J.-S. Tang, C.-F. Li, and G.-C. Guo, Experimental investigation of spectra of dynamical maps and their relation to non-Markovianity, Phys. Rev. Lett. **120**, 060406 (2018).

[44] Z.-D. Liu, H. Lyyra, Y.-N. Sun, B.-H. Liu, C.-F. Li, G.-C. Guo, S. Maniscalco, and J. Piilo, Experimental implementation of fully controlled dephasing dynamics and synthetic spectral densities, Nat. Commun. **9**, 3453 (2018).

[45] G. García-Pérez, M. A. C. Rossi, and S. Maniscalco, IBM Q Experience as a versatile experimental testbed for simulating open quantum systems, Npj Quantum Inf. **6**, 1 (2020).

[46] S. Gröblacher, A. Trubarov, N. Prigge, G. D. Cole, M. Aspelmeyer, and J. Eisert, Observation of non-Markovian micromechanical Brownian motion, Nat. Commun. **6**, 7606 (2015).

[47] J. Nokkala, F. Galve, R. Zambrini, S. Maniscalco, and J. Piilo, Complex quantum networks as structured environments: engineering and probing, Sci. Rep. **6**, 26861 (2016).

[48] R. Menu, J. Langbehn, C. P. Koch, and G. Morigi, Reservoir-engineering shortcuts to adiabaticity, Phys. Rev. Res. **4**, 033005 (2022).

[49] S. Davidson, F. A. Pollock, and E. Gauger, Eliminating radiative losses in long-range exciton transport, PRX Quantum **3**, 020354 (2022).

[50] Y.-S. Ra, A. Dufour, M. Walschaers, C. Jacquard, T. Michel, C. Fabre, and N. Treps, Non-Gaussian quantum states of a multimode light field, Nat. Phys. **16**, 144 (2020).

[51] M. Walschaers, B. Sundar, N. Treps, L. D. Carr, and V. Parigi, Emergent complex quantum networks in continuous-variables non-Gaussian states, Quantum Sci. Technol. **8**, 035009 (2023).

[52] C.-F. Li, G.-C. Guo, and J. Piilo, Non-Markovian quantum dynamics: What is it good for?, Europhys. Lett. **128**, 30001 (2020).

[53] K. Head-Marsden, S. Krastanov, D. A. Mazziotti, and P. Narang, Capturing non-Markovian dynamics on near-term quantum computers, Phys. Rev. Res. **3**, 013182 (2021).

[54] M. Gluza, J. a. Sabino, N. H. Ng, G. Vitagliano, M. Pezzutto, Y. Omar, I. Mazets, M. Huber, J. Schmiedmayer, and J. Eisert, Quantum Field Thermal Machines, PRX Quantum **2**, 030310 (2021).

[55] Y. Shirai, K. Hashimoto, R. Tezuka, C. Uchiyama, and N. Hatano, Non-Markovian effect on quantum Otto engine: Role of system-reservoir interaction, Phys. Rev. Res. **3**, 023078 (2021).

[56] K. G. Paulson, E. Panwar, S. Banerjee, and R. Srikanth, Hierarchy of quantum correlations under non-Markovian dynamics, Quantum Inf. Process. **20**, 141 (2021).

[57] M. Carrega, L. M. Cangemi, G. De Filippis, V. Cataudella, G. Benenti, and M. Sassetti, Engineering dynamical couplings for quantum thermodynamic tasks, PRX Quantum **3**, 010323 (2022).

[58] G. Spaventa, S. F. Huelga, and M. B. Plenio, Capacity of non-Markovianity to boost the efficiency of molecular switches, Phys. Rev. A **105**, 012420 (2022).

[59] With $(\mathbf{q}', \mathbf{p}', q'_S, p'_S)$ the usual quadrature operators of $N+1$ harmonic oscillators, they are defined as $\mathbf{q}^T = \mathbf{q}'^T\sqrt{\Delta_\omega}$; $\mathbf{p}^T = \mathbf{p}'^T\sqrt{\Delta_\omega{}^{-1}}$; $p_S = p'_S\sqrt{\omega_S^{-1}}$; $q_S = q'_S\sqrt{\omega_S}$.

[60] A.-L. Barabási, *Networks Science* (Cambridge University Press, Cambridge, 2016).

[61] M. E. J. Newman, *Networks, Second Edition* (Oxford University Press, Oxford, 2018).

[62] C. Bloch and A. Messiah, The canonical form of an antisymmetric tensor and its application to the theory of superconductivity, Nucl. Phys. **39**, 95 (1962).

[63] D. J. Watts and S. H. Strogatz, Collective dynamics of 'small-world' networks, Nature **393**, 440 (1998).

[64] R. Albert and A.-L. Barabási, Statistical mechanics of complex networks, Rev. Mod. Phys. **74**, 47 (2002).

[65] C. Gardiner and P. Zoller, *Quantum Noise* (Springer Berlin, Heidelberg, 2004).

[66] H.-P. Breuer and F. Petruccione *et al.*, *The Theory of Open Quantum Systems* (Oxford University Press on Demand, Oxford, 2002).

[67] U. Weiss, *Quantum Dissipative Systems* (World Scientific, Singapore, 2008).

[68] F. Mascherpa, A. Smirne, A. D. Somoza, P. Fernández-Acebal, S. Donadi, D. Tamascelli, S. F. Huelga, and M. B. Plenio, Optimized auxiliary oscillators for the simulation of general open quantum systems, Phys. Rev. A **101**, 052108 (2020).

[69] R. Vasile, S. Maniscalco, M. G. Paris, H.-P. Breuer, and J. Piilo, Quantifying non-Markovianity of continuous-variable Gaussian dynamical maps, Phys. Rev. A **84**, 052118 (2011).

[70] G. Ferrini, J. Roslund, F. Arzani, Y. Cai, C. Fabre, and N. Treps, Optimization of networks for measurement-based quantum computation, Phys. Rev. A **91**, 032314 (2015).

[71] A. Monmayrant, S. Weber, and B. Chatel, A newcomer's guide to ultrashort pulse shaping and characterization, J. Phys. B: At., Mol. Opt. Phys. **43**, 103001 (2010).

[72] P. Abdolghader, A. F. Pegoraro, N. Y. Joly, A. Ridsdale, R. Lausten, F. Légaré, and A. Stolow, All normal dispersion nonlinear fibre supercontinuum source characterization and application in hyperspectral stimulated raman scattering microscopy, Opt. Express **28**, 35997 (2020).

[73] F. Arzani, C. Fabre, and N. Treps, Versatile engineering of multimode squeezed states by optimizing the pump spectral profile in spontaneous parametric down-conversion, Phys. Rev. A **97**, 033808 (2018).

[74] T. Kouadou, F. Sansavini, A. Matthieu, H. Johan, N. Treps, and V. Parigi, Spectrally shaped and pulse-by-pulse multiplexed multimode squeezed states of light, Preprint arXiv:2209.10678 (2022).

[75] J. Prior, A. W. Chin, S. F. Huelga, and M. B. Plenio, Efficient simulation of strong system-environment interactions, Phys. Rev. Lett. **105**, 050404 (2010).

[76] A. W. Chin, Á. Rivas, S. F. Huelga, and M. B. Plenio, Exact mapping between system-reservoir quantum models and semi-infinite discrete chains using orthogonal polynomials, J. Math. Phys. **51** (2010).

[77] Y. Tanimura and R. Kubo, Time evolution of a quantum system in contact with a nearly Gaussian-Markoffian noise bath, J. Phys. Soc. Jpn. **58**, 101 (1989).